Effects of wind on forward and turning flight of flying cars using computational fluid dynamics

Taiga Magata[1], Ayato Takii[2], Masashi Yamakawa[1], Yusei Kobayashi[1], Shinichi Asao[3] and Seiichi Takeuchi[3]

[1]Kyoto Institute of Technology, Matsugasaki, Sakyo-ku, Kyoto 606-8585, Japan
m3623028@kit.edu.ac.jp
[2] RIKEN Center for Computational Science, 7-1-26 Minatojima-minami-machi , Chuo-ku, Kobe, Hyogo 650-0047, Japan
[3] College of Industrial Technology, 1-27-1, Amagasaki, Hyogo 661-0047, Japan

Abstract. We have been using various environments and spaces to meet high transportation demands. However, traffic congestion, deteriorating transportation infrastructure, and environmental pollution have become current social problems. To solve these problems, flying vehicles that use near ground space (NGS) are attracting attention. In order to develop such vehicles efficiently, highly accurate computer simulation technology is required. In this study, computer simulations are performed by coupling fluid and rigid body motions using two calculation methods. One is the moving computational domain method, in which the object and computational domain are moved as a single unit to represent the motion of the object and the flow around the body, and the other is the multi-axis sliding mesh method, in which physical quantities are transferred at the boundaries to reproduce the motion of objects with different motions, such as rotating parts. Because the flying car in the development stage is small and has a shape that obtains thrust from multiple propellers, the insertion of disturbances was considered because of the possible effects of wind on the aircraft during actual flight. In this study, we attempted to clarify the effect of wind on the flying car by performing flight simulations in six patterns, one with no wind and the other with a disturbance inserted that causes a headwind during forward flight and a crosswind during turning flight.

Keywords: CFD, Flying Car, turn flight.

1 Introduction

To date, we have used a variety of spaces and environments - above ground, above water, underwater, in the air, and underground - to meet the growing transportation demands of technological development. However, as populations increase around the world, urban traffic congestion, infrastructure deterioration, and environmental

ICCS Camera Ready Version 2024
To cite this paper please use the final published version:
DOI: 10.1007/978-3-031-63749-0_1

pollution have become problems. To address these problems, development of the next generation of air mobility, the flying car, is underway around the world. This flying car is said to use near ground space (NGS), which has not been used in the past, and to significantly reduce noise and exhaust emissions inside the vehicle by installing electric rotors [1]. In addition, various shapes of flying car currently under development are envisioned, most of which are fixed-wing aircraft and rotary-wing aircraft (VTOL) [2]. In particular, many rotary-wing aircraft (VTOLs) in the development stage have many environmental considerations, such as fully electric-driven and hybrid types [3]. Thus, the flying car is a new vehicle that solves current problems.

Flying cars, which are expected to become as common to us as cars, ships, trains, and airplanes in the future, require high safety standards to fly over towns and urban areas. In other words, the design and development of a new flying car airframe requires enormous cost and time. Therefore, various studies on flying cars have been conducted in order to develop actual aircraft more efficiently. Some studies include not only fluid dynamics but also control characteristics, such as wind tunnel tests at high incidence angles using actual propellers [4] and the relationship between VTOL rotors and electric motors in propeller pitch maneuvering [5]. Furthermore, not only research related to actual aircraft testing, but also research related to CFD assuming actual aircraft, such as research on aerodynamic interaction in a two-rotor system with a front rotor and rear rotor assuming a multi-rotor type aircraft [6], and research involving aerodynamic interaction caused by the positional configuration of the propeller [7]. However, most of the studies using CFD have focused on one part of the aircraft or one function, and there have been few reports on numerical flight simulation of eVTOL flight. In response to this current situation, a turning flight simulation [8], which solves the problems of complex attitude changes, acceleration, and long-distance travel that had been considered difficult to solve, and an investigation of the aerodynamic effects on the aircraft's attitude in flight by bringing the propeller to an abrupt stop [9] were conducted. Because these studies were conducted under no-wind conditions, and because many flying cars in the development stage obtain thrust from the rotation of each propeller and are relatively small in length compared to conventional aircraft, there is a new concern that wind will have a large effect during actual flight. Regarding the effect of wind, which has been raised as a new problem, studies have been conducted on stabilization [10] under the influence of wind disturbance for helicopters, which are conventional aircraft. However, the effect of wind on the airframe of an eVTOL, whose rotor diameter is smaller than that of a helicopter, has not been studied because it is still in the early stages of development. Therefore, in this study, forward and turning flight simulations are performed by inserting wind as a disturbance expected during actual flight, in contrast to the previous study of turning flight simulations [8]. In this study, six types of winds up to strong winds on the Beaufort scale (a measure of wind speed) were given as disturbances. This will attempt to clarify the effects of wind on the flight of flying car, which have not been studied before. We believe that this simulation will enable us to understand the effects of wind on airframes in advance of the development of actual airframes, leading to significant reductions in design time and development costs.

This study uses an octorotor-type airframe model with four double-reversing propeller units as the flying car. The flying car flight simulation uses the forward Euler method

ICCS Camera Ready Version 2024
To cite this paper please use the final published version:
DOI: 10.1007/978-3-031-63749-0_1

and Crank-Nicolson method of discretization. At each time step, the motion of the aircraft is calculated using the governing equations of the rigid body, followed by a weakly coupled simulation in which the flow field around the flying car is solved using the governing equations of the fluid. In addition, the moving compu- tational domain (MCD) method [12] based on the unstructured moving grid finite volume method [11], which not only allows for complex motions but also eliminates the need for space constraints. To compute the relative motion between objects with this MCD method, physical quantities are transferred at the boundaries, and the sliding mesh method [13] is used in combination to reproduce the motion of objects with different motions, such as rotating parts. This method not only reproduces the rotation of a flying car's propeller, but also enables the transmission of physical quantities generated by the propeller's rotational motion. The computations were conducted under the unstructured parallel computational environment [14].

The objective of this study is to establish computer simulation as a new method to solve the problem of developing a new flying car by using CFD to reproduce realistic phenomena.

2 Numerical Approach

2.1 Fundamental Equation of Fluid

The three-dimensional Euler equation, which is the basic equation for a non-viscous compressible fluid, is used as the Fundamental equation of fluid from the viewpoint of computational efficiency. The three-dimensional Euler equation:

$$\frac{\partial \boldsymbol{q}}{\partial t}+\frac{\partial \boldsymbol{E}}{\partial x}+\frac{\partial \boldsymbol{F}}{\partial y}+\frac{\partial \boldsymbol{G}}{\partial z}=0, \tag{1}$$

$$\boldsymbol{q}=\begin{pmatrix}\rho\\ \rho u\\ \rho v\\ \rho w\\ e\end{pmatrix}, \boldsymbol{E}=\begin{pmatrix}\rho u\\ \rho u^2+p\\ \rho uv\\ \rho uw\\ u(e+p)\end{pmatrix}, \boldsymbol{F}=\begin{pmatrix}\rho v\\ \rho uv\\ \rho v^2+p\\ \rho vw\\ v(e+p)\end{pmatrix}, \boldsymbol{G}=\begin{pmatrix}\rho v\\ \rho uv\\ \rho v^2+p\\ \rho vw\\ v(e+p)\end{pmatrix} \tag{2}$$

where $\boldsymbol{q}$ is the conserved quantity vector and $\boldsymbol{E}, \boldsymbol{F}, \boldsymbol{G}$ are the inviscid flux vectors in the x, y, z directions. ρ is the density of the fluid, u, v, w are the velocity components in the x, y, z directions, and e is the total energy per unit volume. However, the above equation is dimensionless. The p in equation (2) is the pressure of the gas, which can be obtained by the equation of state of an ideal gas shown in equation (3) when the gas is assumed to be an ideal gas. Note that γ is the specific heat ratio.

$$p=(\gamma-1)\left\{e-\frac{1}{2}\rho(u^2+v^2+w^2)\right\} \tag{3}$$

In this study, the specific heat ratio was set to 1.4 because the air temperature was set to 10[°C].

ICCS Camera Ready Version 2024
To cite this paper please use the final published version:
DOI: 10.1007/978-3-031-63749-0_1

2.2 Fundamental Equation of Rigid Body

The three-dimensional Newton-Euler equation is used as the governing fundamental equation of rigid body to represent translational and rotational motion in three-dimensional space. The three-dimensional Newton-Euler equation:

$$m\frac{d\ddot{\boldsymbol{r}}}{dt^2} = \boldsymbol{f} \tag{4}$$

$$\boldsymbol{I}\frac{d\dot{\boldsymbol{\omega}}}{dt} + \boldsymbol{\omega} \times I\boldsymbol{\omega} = \boldsymbol{T} \tag{5}$$

where m is the mass of the rigid body and $\boldsymbol{I}$ is the inertia tensor. In addition, r, f, ω and T represent the position vector, external force vector, angular velocity vector, and torque vector in three-dimensional space, respectively. However, because the flying car used in this research has no moving parts other than the propeller, the aircraft is assumed to be a rigid body with a constant center of gravity. The equations in the previous section and the above equation are computed coupled to simulate the six degrees of freedom.

2.3 Moving computational domain approach

The calculations are performed using a moving computational domain method [12] based on the unstructured moving lattice finite volume method [11]. A schematic diagram of the moving computational domain method is shown in Figure 1. This method makes it possible to move the computational domain along with the object, thus eliminating restrictions due to the size of the computational domain. In other words, this method allows objects to move in an infinite region. In addition, it satisfies each of the following two problems that are often encountered when dealing with moving boundary problems.

· Strictly satisfying the conservation law of the fluid on all moving computational grids.

· To reproduce the moving boundary while maintaining the computational grid geometry for highly accurate fluid calculations.

As shown above, the moving computational domain method enables calculations that strictly satisfy the geometric conservation law even when the lattice moves.

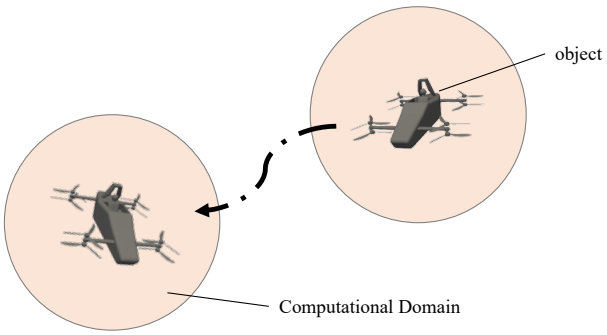

Fig.1. Moving Computational Domain Method

ICCS Camera Ready Version 2024
To cite this paper please use the final published version:
DOI: 10.1007/978-3-031-63749-0_1

2.4 Multi-axis Sliding Mesh Approach

The MCD method enables the representation of free motion of an object by moving the computational domain along with the object. However, the flying car used in this study is an octorotor-type airframe model with four double-reversing propeller units, so it is necessary to represent the relative motion between multiple objects on a boundary-fitted grid. Therefore, the sliding mesh method[13] has been used to arbitrarily divide a region and slide the regions on the boundary surface. In particular, the multi-axis sliding mesh method corresponds to the region segmentation with multiple rotation axes of the sliding mesh method. The simplicity of the algorithm of this method reduces the computational load and satisfies the user without overlapping computational domains. Figure 2 shows a schematic of the multi-axis sliding mesh method, which divides a region with multiple rotation axes. In this study, the multi-axis sliding mesh method shown in Figure 2 was used to reproduce the rotation of the rotor. Specifically, as shown in Figure 3, eight rotor regions are provided for the fuselage region to make up the overall calculation region. In addition, this research can not only reproduce the rotational motion of a flying car by the multi-axis sliding mesh method, but also realize the physical quantity transfer obtained by the rotational motion.

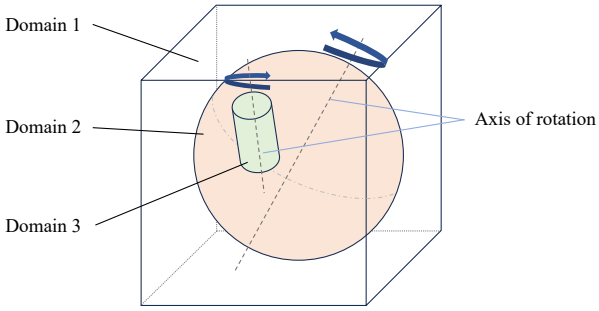

Fig.2. Conceptual Diagram of Multi-axis Sliding Mesh Method

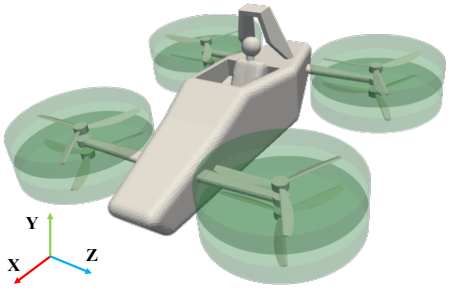

Fig.3. Flying car model and Sliding mesh interface

ICCS Camera Ready Version 2024
To cite this paper please use the final published version:
DOI: 10.1007/978-3-031-63749-0_1

3 Simulation Summary

3.1 Flight Simulation Conditions

In this study, a total of seven forward and turning flight simulations were performed under no-wind conditions and with six different winds inserted as expected disturbances during actual flight. Two types of flight simulation conditions are shown below. The first type is a simulation overview of an Acceleration turning flight when the aircraft continues to accelerate its speed after transitioning from forward flight to a turn. The second type is constant velocity turning flight, in which the aircraft is controlled to track the target speed after transitioning from forward flight to turning flight. In both simulations, the wind is set to be headwind during forward flight. Since the turning flight is directed toward the negative direction of the z-axis, the crosswind is in the direction that agitates the turning motion during the turning flight.

· Acceleration turning flight

1) The initial conditions are either no wind or a constant wind blowing in the negative direction along the x-axis.
2) The target speed of 60 km/h is given in the x-axis direction.
3) As soon as the difference between the forward speed of the aircraft and the target speed is less than 2 km/h, the target angle in the roll direction is set to 30 degrees and the aircraft begins to turn.
4) The acceleration during forward flight is continued after the transition to turning flight.
5) The aircraft performs a turning flight and ends the turning flight when the yaw angle exceeds 90 degrees.

· Constant velocity turning flight

1) The initial conditions are either no wind or a constant wind blowing in the negative direction along the x-axis.
2) The target speed of 60 km/h is given in the x-axis direction.
3) As soon as the difference between the forward speed of the aircraft and the target speed is less than 2 km/h, the target angle in the roll direction is set to 30 degrees and the aircraft begins to turn.
4) After the turning flight transition, the aircraft continues to maintain the target forward speed of 60 km/h.
5) The aircraft performs a turning flight and ends the turning flight when the yaw angle exceeds 90 degrees.

However, the initial conditions in (1) are six types of wind given as disturbances in 10 km/h increments from 10 km/h to 60 km/h, and no wind conditions, for a total of seven patterns.

3.2 Computation Model

Figure 4 shows the computational domain of the airframe and the area around the airframe. The spherical computational domain is approximately 30 times larger than the total length of the aircraft, which is the characteristic length, to account for the

ICCS Camera Ready Version 2024
To cite this paper please use the final published version:
DOI: 10.1007/978-3-031-63749-0_1

downwash effect caused by the propellers. As shown in Figure 4, the grids around the aircraft are finely detailed so that the flow field around the aircraft can be obtained with high accuracy. Figure 5(a) shows the computational model of the oct-rotor machine with four pairs of eight double-reversing rotors used in this simulation. Figure 5(b) shows the computational grid corresponding to the rotor area propeller locations shown in Figure 3. However, this model was created based on the Japanese SkyDrive's SD-03[15]. The model was created with an overall length of 4 m and a weight of 400 kg. The overall length of the aircraft was used as a characteristic length for the calculations in the simulations. As shown in Figure 4, the computational model used in this study is an unstructured lattice and was created using MEGG3D [16][17]. In addition, the total lattice count is about 3 million, and each propeller lattice count is about 120 thousand. The minimum lattice width on the calculated lattice is approximately 6 [mm] of the rotor surface.

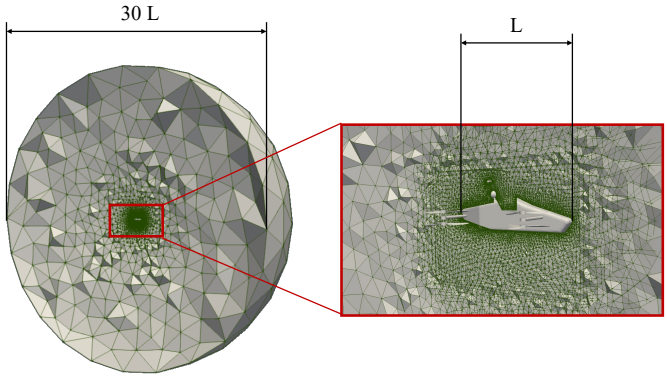

Fig.4. Computational domain and grid size around the Flying car model

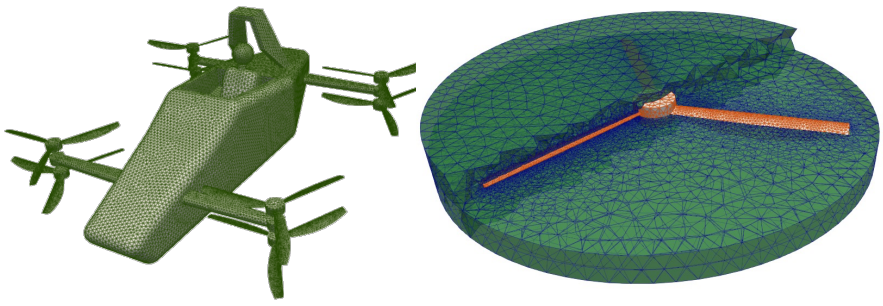

(a) Surface mesh of the flying car (b) Propeller domain

Fig.5. Surface grid of Flying car model

3.3 Calculation Conditions

Table 1 shows characteristic values for this simulation. Characteristic length, density, and velocity are shown as characteristic values. The characteristic length is the total

ICCS Camera Ready Version 2024
To cite this paper please use the final published version:
DOI: 10.1007/978-3-031-63749-0_1

length of the aircraft as shown in Figure 4, the characteristic density is the density of the air, and the characteristic speed is the speed of sound. Table 2 shows the wind speeds u, v and w given as initial conditions in the x, y and z axes. The wind speeds v and w on the y and z axes were 0 km/h. The wind speed u on the x axis was given as no wind (0 km/h) or six different wind speeds from 10 km/h to 60 km/h in the negative direction of the x-axis at 10 km/h intervals, for a total of seven simulation patterns. Table 3 shows the boundary conditions for this simulation. Three types of boundary conditions are set: a slip wall boundary, a Riemann invariant boundary condition, and a sliding mesh interface using the sliding mesh method.

Table 1. Characteristic values

Density of the air	1.247 [kg/m^3]
Characteristic velocity	340.29 [m/s]
Characteristic length	4.0 [m]

Table 2. Initial condition

u	0, -10 ~ -60 [km/h]
v	0 [km/h]
w	0 [km/h]

Table 3. Boundary condition

Aircraft surface	Slip wall condition
Outer boundary	Riemann invariant boundary condition
Other boundary	Sliding mesh interface

3.4 Attitude control

The model used in this simulation represents the rotation of the aircraft in pitch and roll direction by the difference in thrust between the front-back and left-right directions. The yaw rotation of the aircraft is expressed by using the counter-torque generated by the rotation of the propeller [18]. Therefore, control is performed by the difference in propeller speed. Figure 6 shows how the posture is controlled by the different number of rotations to reproduce each operation. However, the throttle, aileron, rudder, and elevator shown in Figure 6 represent operations to raise and lower the aircraft and to promote rolling, yawing, and pitching of the aircraft. The model used in this study, which was created based on the Japanese SkyDrive SD-03 [15], is based on a rotational speed of 1930 rpm when hovering. Figure 7 shows the direction of rotation of each propeller (clockwise : CW, counter-clockwise : CCW).

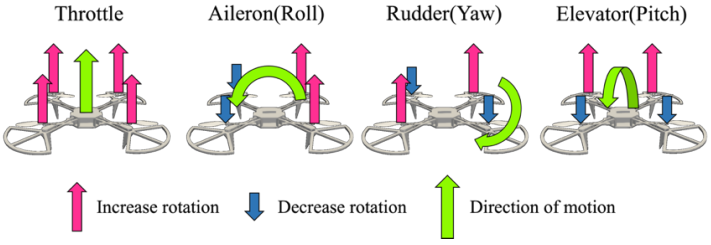

Fig.6. Attitude control by rotation speed

ICCS Camera Ready Version 2024
To cite this paper please use the final published version:
DOI: 10.1007/978-3-031-63749-0_1

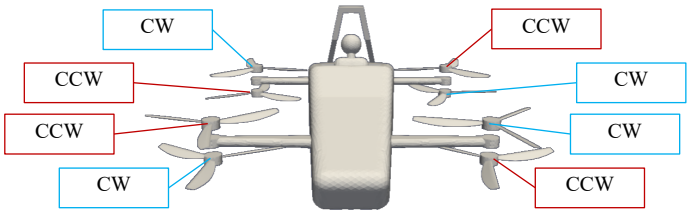

Fig.7. Rotation direction of each propeller

4 Simulation Results

4.1 Forward flight simulation

The results of the aircraft's forward flight toward the target forward speed of 60 km/h are shown in this section. Figure 8 shows a graph of the relationship between time and aircraft forward speed. Simulation results of (a) an acceleration turning flight and (b) a constant velocity turning flight to follow the target speed of 60 km/h are shown in (a) and (b), respectively. The simulation results are for the no-wind condition and for a constant wind speed of 10 km/h to 60 km/h in 10 km/h increments along the negative x-axis, respectively. Figure 8 shows that the time to reach the target speed of 60 km/h in the forward direction is slowed down as the headwind is increased in both results. Figure 8(b) shows that the target speed is maintained near 60 km/h compared to (a), indicating that the constant velocity turning flight can be reproduced.

Figures 9(a) and (b) show the results for no wind and a constant wind speed of 60 km/h for the negative x-axis, respectively, and the visualization results during forward flight with the velocity isosurface of 25 m/s displayed for each result. Figure 9 is presented in dimensionless quantities for consistency with other papers. The dimensioned quantities can be calculated using the characteristic values in Table 1. From the comparison in Figure 9, it can be confirmed that the flow in front of the fuselage in (b) is unstable due to disturbance, even though the fuselage pitch angle is controlled to be 15 deg during forward flight and the projected area from the front of the fuselage is equal.

Furthermore, in order to quantitatively evaluate the effect of wind during forward flight, a comparison of the drag force acting on the airframe during forward flight is performed for each simulation result. The drag force F:

$$F = T\sin\theta - F_x \tag{6}$$

where T is the thrust generated by the eight propellers, θ is the pitch angle of the aircraft in forward flight, and F_x is the force applied in the direction of the x axis of the aircraft. The thrust T is obtained by the propeller specific value A and the propeller speed n as in equation (7).

$$T = An^2 \tag{7}$$

Figure 10 shows the relationship between time and x-axis force F_x during forward flight. Figure 10 shows that the force F_x in the x-axis direction decreases as the disturbance is increased. Table 4 shows the average values of the force F_x in the x-axis direction from 4 to 8[s], the average values of the thrust force $T\sin\theta$ from 4 to 8[s], and the

ICCS Camera Ready Version 2024
To cite this paper please use the final published version:
DOI: 10.1007/978-3-031-63749-0_1

drag force F calculated from formula (6) using each average value. Comparing the results for the no-wind condition and the 60 km/h disturbance, Table 4 shows that the force F_x in the x-axis direction is reduced by 26.8% due to the headwind. This decrease in force F_x in the x-axis direction is thought to have slowed the time to reach the target speed as shown in Figure 9. It was also confirmed that the drag force exerted on the aircraft during forward flight in no-wind conditions acts 349[N]. From the drag force during forward flight in no wind, the force F_{wing} exerted by the wind on the aircraft is calculated using equation (8).

$$F_{wing} = F_i - F_0 \tag{8}$$

F_i is the drag force F calculated by substituting the force F_x for the constant wind disturbance of 10 km/h to 60 km/h in the negative direction of the x-axis into equation (6), and F_0 is the drag force F calculated from the force F_x in the no wind condition into equation (6). Table 5 shows the force F_{wing} exerted on the aircraft by the wind calculated from equation (8). From Table 5, the increase in force to force F_{60}, calculated from the force F_{10} when subjected to a disturbance of 10 km/h, was obtained as 374%. The above confirms that the wind exerts a pressure of 56.6[P_a] on a projected area of 2.42[m^2] from the forward direction during high winds in the Beaufort scale.

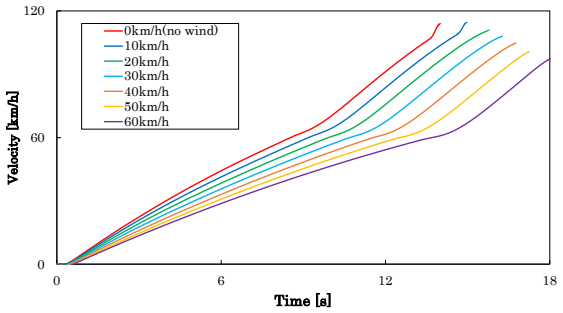

(a) Acceleration turning flight

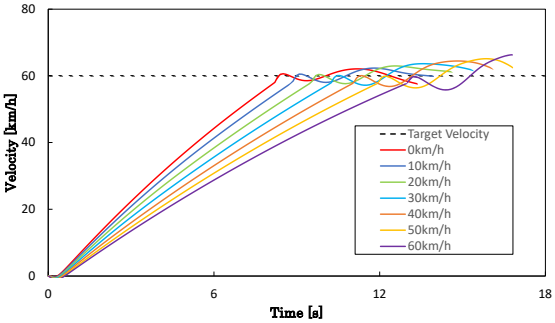

(b) Constant velocity turning flight

Fig.8. Time and aircraft forward speed

ICCS Camera Ready Version 2024
To cite this paper please use the final published version:
DOI: 10.1007/978-3-031-63749-0_1

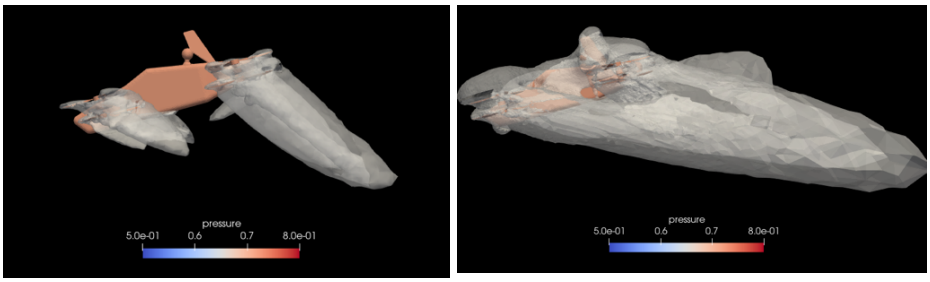

(a) Simulation results in no wind. (b) Simulation results for disturbance at 60 km/h

Fig.9. Visualization of velocity isosurfaces during forward flight

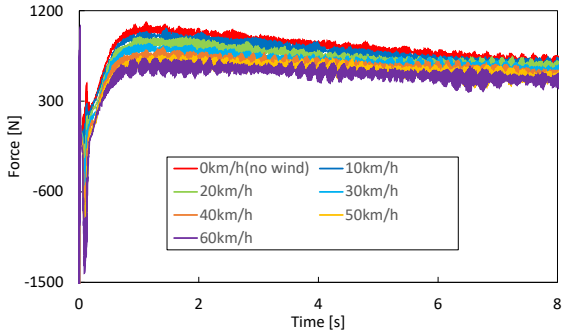

Fig. 10. Force in the forward direction of the aircraft.

Table 4. Various forces generated by each simulation

v [km/h]	0	10	20	30	40	50	60
$T\sin\theta$ [N]	1115	1101	1086	1070	1057	1046	1039
F_x [N]	766	723	684	652	620	587	552
F [N]	349	378	402	419	436	459	487

Table 5. Drag force on the aircraft and the rate of increase of that drag force

v [km/h]	10	20	30	40	50	60
F_x [N]	28.9	52.2	69.4	87.1	110	137
Rate of increase [%]	0.0	80.6	140	201	281	374

4.2 Acceleration turning flight

As soon as the difference between the forward speed of the aircraft and the target speed is less than 2 km/h, the target angle in the roll direction is set to 30 degrees and the aircraft begins to turn. Accelerated turning flight simulation results are shown in this section when acceleration is continued after turning flight as it was during forward flight. Figure 11 shows a graph of the flight trajectory of a turning aircraft viewed from above with the x-axis on the horizontal axis and the z-axis on the vertical axis. Figure 11 shows the simulation results when no wind or a constant wind speed of 10 km/h to 60 km/h is applied as a disturbance in the negative x-axis direction, respectively. In addition, the trajectory of the turning flight in Figure 11 shows a forward flight in the

ICCS Camera Ready Version 2024
To cite this paper please use the final published version:
DOI: 10.1007/978-3-031-63749-0_1

positive direction from 0 on the x-axis and then a turning flight in the negative direction on the z-axis. The results of each trajectory are overlaid for comparison. Figure 11 shows that the turn diameter decreases as the constant wind speed given as a disturbance is increased. Furthermore, it can be seen that the distance traveled by the aircraft is shortening after the turning flight transition. The results show that the plane moved 120[m] along the negative z-axis after turning in the no-wind condition and 72.4[m] along the negative z-axis when a disturbance of 60 km/h was applied. When a disturbance of 60 km/h was applied, the distance traveled after the turn was 39.7% less than that for a turning flight in no wind conditions. The reason for this is considered to be that the Yaw angle of 90[deg], which is the condition for the end of the turning flight, was reached early because the disturbance wind was set in the direction that agitated the turning flight.

Figures 12(a) and (b) show the results for no wind and a constant wind speed of 60 km/h for the negative x-axis, respectively, and the visualization results during turning flight with the velocity isosurface of 25 m/s displayed for each result. Figure 12 is presented in dimensionless quantities for consistency with other papers. The dimensioned quantities can be calculated using the characteristic values in Table 1. After the turning flight transition, the wind is set to agitate the turning, and it can be confirmed that the results for a disturbance of 60 km/h have an effect on the flow toward the side of the aircraft compared to the no-wind condition. In addition, the continued acceleration of the aircraft's forward speed after the turning flight transition also confirms the turbulence of the flow in front of the aircraft.

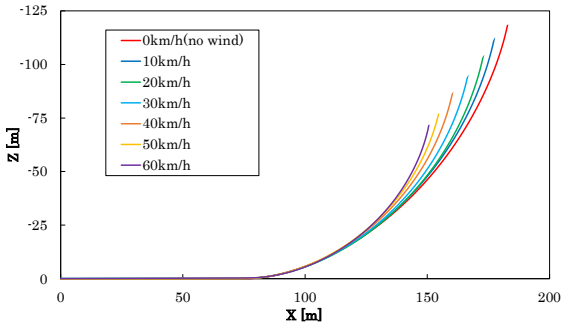

Fig. 11. Flight trajectory during acceleration turn flight

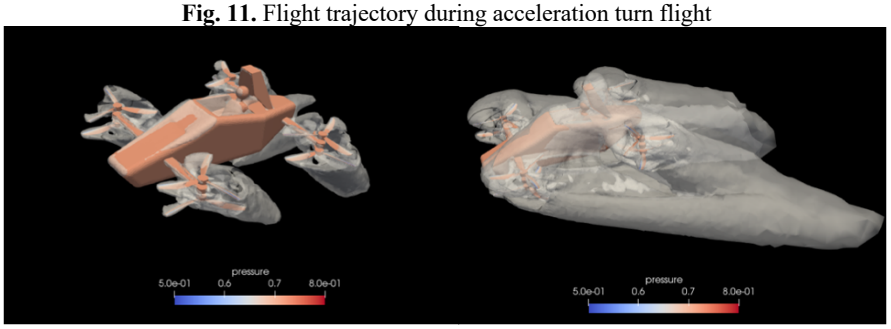

(a) Simulation results in no wind (b) Simulation results for disturbance at 60 km/h

Fig. 12. Visualization of velocity isosurfaces during sharp turn flight

ICCS Camera Ready Version 2024
To cite this paper please use the final published version:
DOI: 10.1007/978-3-031-63749-0_1

4.3 Constant velocity turning flight

This section shows the results of a constant velocity turning flight simulation in which the aircraft was controlled to maintain its speed in the direction of travel at 60 km/h, which was given as the target speed during forward flight, even after the turning flight. Figure 13 shows a graph of the trajectory of a turning aircraft viewed from above with the x-axis on the horizontal axis and the z-axis on the vertical axis. As in Figure 11, Figure 13 shows the simulation results when no wind or a constant wind speed of 10 km/h to 60 km/h is applied as a disturbance in the negative x-axis direction, respectively. In addition, each trajectory result is overlaid for comparison. When constant velocity turning flight was used, there was no difference in the distance traveled in the negative direction of the z-axis after turning flight compared to acceleration turning flight.

Therefore, to quantify the effect of disturbance during constant-speed turning flight, differences in rotation speed are compared. Figure 14 is a zoomed-in plot of only the rotation speed results for each simulation result during constant-speed turning flight. From Figure 14, it was observed that a large rotation speed amplitude was drawn when the flight transitioned to a turning flight. In particular, the amplitude of the results for a constant wind speed of 20 km/h to 60 km/h is smaller than that for the no-wind condition. The reason for this is thought to be that the wind was inserted as a disturbance in the direction that agitated the circling flight, which facilitated the transition to the circling flight. The amplitude of the rotation speed when 10 km/h was given as a disturbance was larger than that in the no-wind condition, and the amplitude of the rotation speed did not decrease proportionally as the disturbance increased. The reason for this is considered to be the influence of the control. In this study, the rotation speed is calculated by the proportional - derivative (PD) controller using thrust and angular velocities for roll, pitch, and yaw for the three axes as control inputs. The control gains in the PD control are considered to be inappropriate. Furthermore, the control gains may also be the reason why the forward speed of the aircraft in Figure 8(b) did not completely follow the target speed.

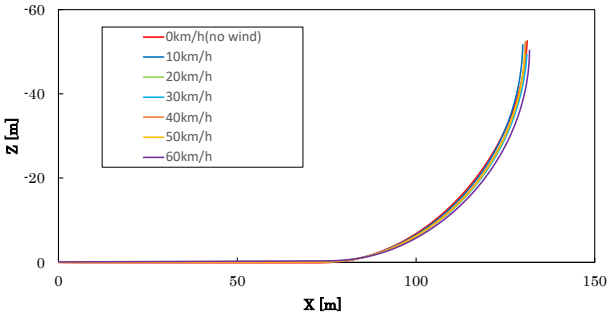

Fig. 13. Flight trajectory at constant speed turning

ICCS Camera Ready Version 2024
To cite this paper please use the final published version:
DOI: 10.1007/978-3-031-63749-0_1

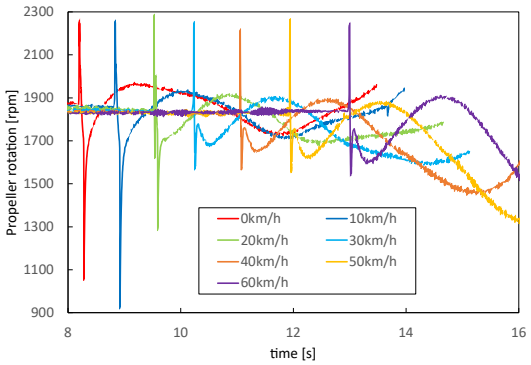

Fig.14. Rotation speed during turning flight

5 Conclusions

The MCD method and the multi-axis sliding mesh method were used together to not only reproduce the motion of the propeller, but also to reproduce forward and turning flight by solving the flow field around the flying car's fuselage. The challenges of complex attitude change, acceleration, and long-distance travel, which had been considered difficult, were solved, and disturbances, which had not been considered previously, were successfully inserted. These results confirm that the time required to reach the target forward speed increases when a headwind disturbance is applied to the aircraft during forward flight. The simulation results also confirmed the reproduction of a headwind by calculating the force in the x-axis direction during forward flight, the thrust by the propeller, and the drag force exerted by the wind on the fuselage. In addition, two patterns of circling flight were simulated: acceleration turning flight, in which acceleration is continued after the circling flight transition, and constant velocity turning flight, in which turning is performed at a constant speed. In the acceleration turning simulation, the crosswind was set to agitate the turning motion, resulting in a turning trajectory that achieves a yaw angle of 90deg faster as the disturbance is increased. In constant velocity turning flight, the turning trajectory was compared to the RPM during the turning flight, suggesting that the control gain used for PD control was inappropriate for constant velocity turning flight. Future prospects include the development of a control design and simulation environment that can perfectly follow the set forward and turning flight trajectories.

Acknowledgments. This paper is based on results obtained from a project, JPNP14004, subsidized by the New Energy and Industrial Technology Development Organization (NEDO).

References

1. G. Pan and M.-S. Alouini : Flying Car Transportation System: Advances, Techniques, and Challenges. IEEE Access (Volume: 9), 24586 - 24603 (2021).

ICCS Camera Ready Version 2024
To cite this paper please use the final published version:
DOI: 10.1007/978-3-031-63749-0_1

2. Rostami, M., Bardin, J., Neufeld, D., Chung, J.: EVTOL Tilt-Wing Aircraft Design under Uncertainty Using a Multidisciplinary Possibilistic Approach, Aerospace 2023, 10, 718.
3. Ugwueze, O., Statheros, T., Bromfield, M.A., Horri, N. : Trends in eVTOL aircraft development : The Concepts, Enablers and Challenges. In Proceedings of the AIAA SCITECH 2023 Forum, National Harbor, MD, USA, 23–27 January 2023.
4. Simmons, B. M., Hatke, D. B., : Investigation of High Incidence Angle Propeller Aerodynamics for Subscale eVTOL Aircraft. NASA TM–20210014010, May 2021.
5. M. D. Pavel : Understanding the control characteristics of electric vertical take-off and landing (eVTOL) aircraft for urban air mobility, Aerospace Science and Technology(2021) 107143.
6. R. Healy, M. Misiorowski, F. Gandhi: A Systematic CFD-Based Examination of Rotor-Rotor Separation Effects on Interactional Aerodynamics for Large eVTOL Aircraft. in Proceedings of the 75th Annual Forum, (Philadelphia), VFS International, May 2019.
7. Zanotti A., Piccinini R., Tugnoli M. : Numerical Investigation of the Rotor-Rotor Aerodynamic interaction of evtol configurations by a mid-fidelity approach. In Proceedings of the 47th European Rotorcraft Forum, Virtual Event, September 7-9 2021.
8. TAKII, A. et al.," Turning Flight Simulation with Fluid-Rigid Body Interaction for Flying Car with Contra-Rotating Propellers," ICCS (2023), pp. 566–577
9. NAOYA T. et al.," Numerical Simulation of the Octorotor Flying Car in Sudden Rotor Stop," ICCS (2023), pp. 33-46 .
10. Kumeresan A. Danapalasingam et al. : Robust helicopter stabilization in the face of wind disturbance. 49th IEEE Conference on Decision and Control, pp. 3832-3837, (2010).
11. Yamakawa, M. et al. : Numerical Simulation for a Flow around Body Ejection using an Axisymmetric Unstructured Moving Grid Method, Computational Thermal Sciences, Vol.4, No.3, pp.217-223(2012)
12. Yamakawa, M. et al. : Numerical Simulation of Rotation of Intermeshing Rotors using Added and Eliminated Mesh Method, Procedia Computer Science, Volume 108, pp.1883-1892(2017)
13. Takii, A., Yamakawa, M., Asao, S., Tajiri, K.: Six degrees of freedom flight simulation of tilt-rotor aircraft with nacelle conversion. Journal of Computational Science, 44, 101164 (2020).
14. Yamakawa, M. et al. : Domain decomposition method for unstructured meshes in an OpenMP computing environment, Computers & Fluids, Vol. 45, pp.168-171(2011)
15. SkyDrive Inc Homepage. https://en.skydrive2020.com/. Accessed 23 Jan 2023.
16. Ito,Y.,Nakahashi,K.:Surfacetriangulationforpolygonalmodelsbasedon CADdata.In- ternational Journal for Numerical Methods in Fluids, 39(1), 75-96 (2002).
17. Ito, Y.: Challenges in unstructured mesh generation for practical and efficient computational fluid dynamics simulations. Comput Fluids 85(1):47–52 (2013).
18. Gomi,R.,Takii,A.,Yamakawa,M.,Asao,S.,Takeuchi,S.,Nishimura,M.:Flightsimula-tion-from takeoff to yawing of eVTOL airplane with coaxial propellers by fluid-rigid body interaction. Advances in Aerodynamics, 5(1), 1-15 (2023).

ICCS Camera Ready Version 2024
To cite this paper please use the final published version:
DOI: 10.1007/978-3-031-63749-0_1